

ARTICLE OPEN



Iron-rich talc as air-stable platform for magnetic two-dimensional materials

Aleksandar Matković¹✉, Lukas Ludescher¹, Oleg E. Peil², Apoorva Sharma³, Kevin-P. Gradwohl¹, Markus Kratzer¹, Maik Zimmermann⁴, Jakob Genser⁵, Daniel Knez⁶, Evelin Fisslthaler⁷, Christoph Gammer⁸, Alois Lugstein⁵, Ronald J. Bakker⁴, Lorenz Romaner², Dietrich R. T. Zahn^{3,9}, Ferdinand Hofer^{6,7}, Georgeta Salvan^{3,9}, Johann G. Raith⁴ and Christian Teichert¹✉

Intrinsically magnetic layered materials – especially monolayers – suffer from the lack of ambient stability and mostly exhibit magnetic ordering only at cryogenic temperatures. These restraints impose a great challenge for the integration of two-dimensional magnetic materials into future technologies. We propose to overcome this by exploiting phyllosilicates, such as iron-rich talc. Via combined magnetic force microscopy in applied external magnetic fields, superconducting quantum interference device magnetometry, first-principle calculations, and structural analysis, we demonstrate that incorporated iron ions in talc are in a very robust high spin state, resulting in a weak ferromagnetic behavior at room temperature. Iron-rich talc can be thinned down to a monolayer, remaining fully stable under ambient conditions, and retaining magnetic properties even in monolayers. Finally, we propose iron-rich end members of the phyllosilicates as very promising platforms for air-stable magnetic monolayers.

npj 2D Materials and Applications (2021)5:94; <https://doi.org/10.1038/s41699-021-00276-3>

INTRODUCTION

Starting from graphene¹, many other two-dimensional (2D) van der Waals (vdW) materials have been isolated as monolayers, demonstrating extraordinary electrical, mechanical, and optical properties^{2–7}. Since intrinsic magnetic ordering in 2D materials was not observed for over a decade, efforts were made to induce magnetic ordering in originally non-magnetic 2D materials, mainly relying on defect engineering, proximity effects, and doping/alloying^{8–15}. The first observations of intrinsic 2D ferromagnetism were reported for CrI₃ and Cr₂Ge₂Te₆^{16,17}, and many other vdW materials with intrinsic magnetism have been reported ever since^{18–23}. These systems open a whole field of possibilities to retain a ferromagnetic or antiferromagnetic ground state in a monolayer and at finite temperatures^{16–23}. The main importance of intrinsic magnetism lies in the fact that these materials can be readily integrated into heterostructures^{18,21}, providing unparalleled opportunities in the fields of 2D-spintronics, data storage, magnetoelectronics, and magneto-optics^{19–21,24–29}. However, most of the explored magnetic 2D materials are lacking ambient stability^{17,21–24,30,31}.

To reach the full potential that intrinsic 2D magnetic materials have to offer they must be air-stable even in monolayers, and the critical ordering temperature must be above room temperature. This will allow straightforward processing and integration into devices, opening a vast field of applications for 2D magnets^{19,21,24–29}. To achieve these goals, one of the most promising pathways that has emerged relies on the introduction of small quantities of magnetic dopants as iron (Fe), cobalt (Co), or vanadium (V) into usually diamagnetic vdW material hosts to form dilute magnetic layered systems^{14,15,31–36}. Within these alloyed monolayers, room-temperature ferromagnetic ordering was achieved and – in most cases – exhibited sufficient ambient stability^{14,15,31–36}. Especially, V

and Fe alloying³² with transition metal dichalcogenides as MoS₂, WS₂, and WSe₂ provide a very reliable pathway to achieve and tune ferromagnetic response at room temperature^{14,15,34–36}. However, dilute magnetic monolayer systems depend on precisely controlled dopant concentrations and are hard to realize as multi-layer structures.

In comparison to dilute magnetic monolayers, naturally occurring magnetic layered materials provide many parallels while they overcome at the same time the above-mentioned obstacles, therefore, offering an alternative pathway for air-stable tailored 2D magnetic materials. For instance, iron oxyhalides have been theoretically anticipated as potential air-stable candidates³⁷. In addition, naturally occurring sulfosalt cylindrite with vdW superlattice was proposed as potential air-stable 2D magnetic material³⁸. While it is possible to exfoliate monolayers, the bulk critical ordering temperature was found to be below 20 K³⁸.

In this study, we propose phyllosilicates as a novel class of 2D magnetic materials that satisfy the above-mentioned criterion of ambient stability and provide a platform for the integration of the local-moment bearing ions into their monolayers. Phyllosilicates – vdW materials with parallel double sheets of (Si/Al)₄O₁₀ tetrahedra – are one of the major types of silicates, with over 240 minerals falling into this group^{39,40}. The complexity of the phyllosilicate structure enables a high degree of variability³⁹. In particular, the incorporation of other elements like Fe or Co is of special interest for layered magnetic materials^{41,42}. Bulk Fe-rich phyllosilicates – such as minnesotaite and annite – have been reported to have magnetic moments in-plane, commonly exhibiting layered anti-ferromagnetism⁴¹. Further, synthetic crystals of fluorophlogopite mica were demonstrated to exhibit paramagnetic response at low temperatures, which was associated to incorporated iron⁴³. We consider the case of iron-rich mono- and multi-layer crystalline

¹Institute of Physics, Montanuniversität Leoben, 8700 Leoben, Austria. ²Materials Center Leoben Forschung GmbH (MCL), 8700 Leoben, Austria. ³Semiconductor Physics, Chemnitz University of Technology, D-09107 Chemnitz, Germany. ⁴Chair of Resource Mineralogy, Montanuniversität Leoben, 8700 Leoben, Austria. ⁵Institute for Solid State Electronics, Technische Universität Wien, 1040 Vienna, Austria. ⁶Institute of Electron Microscopy and Nanoanalysis (FELMI), Graz University of Technology, 8010 Graz, Austria. ⁷Graz Centre for Electron Microscopy (ZFE), 8010 Graz, Austria. ⁸Erich Schmid Institute of Materials Science, Austrian Academy of Sciences, 8700 Leoben, Austria. ⁹Center for Materials, Architecture, and Integration of Nanomembranes (MAIN), Chemnitz University of Technology, 09126 Chemnitz, Germany.

✉email: aleksandar.matkovic@unileoben.ac.at; teichert@unileoben.ac.at

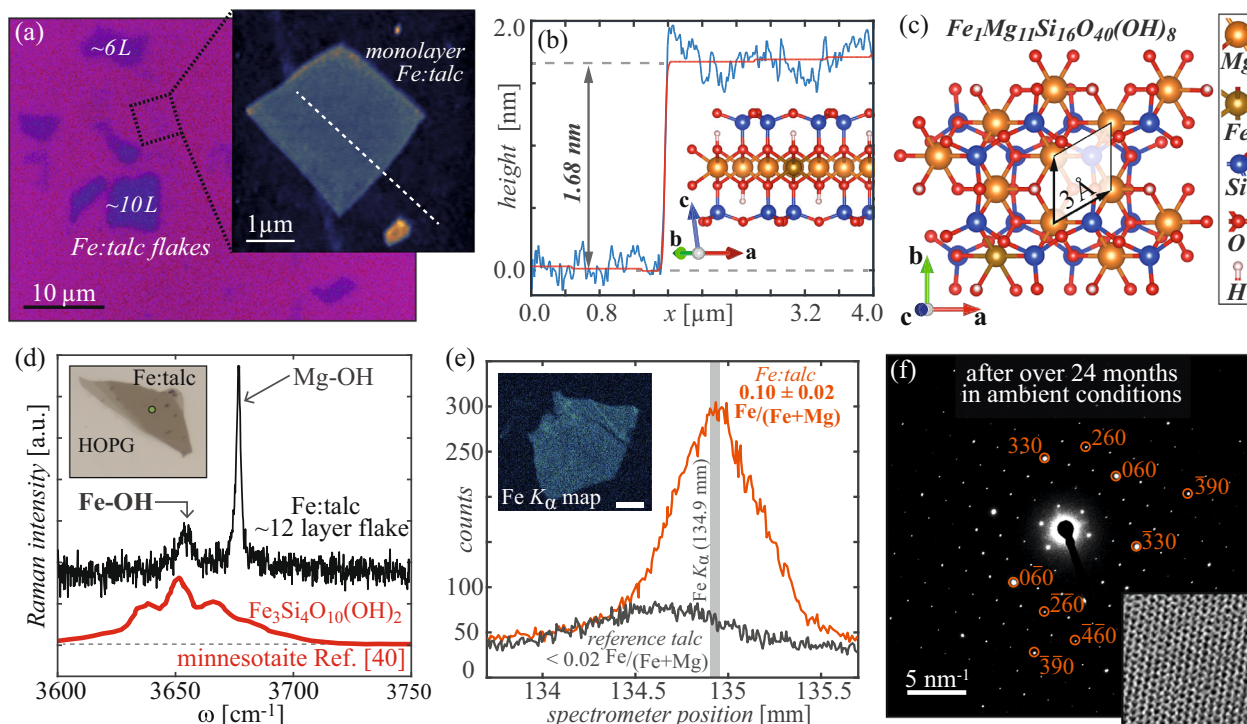


Fig. 1 Fe:talc structural analysis. **a** Optical micrograph of several Fe:talc flakes on SiO₂/Si substrate (300 nm SiO₂ layer) also indicates the estimated number of layers for the thicker flakes. Inset of **a** presents AFM topography image of a monolayer Fe:talc (5 × 5 μm², z = 6 nm) indicated in **a** by the dotted black square. **b** Height cross section (blue line) along the dashed white line in the inset of **a** and the fitted height profile (red line), also showing a side view of the Fe:talc structure. **c** Crystal structure of a monolayer of Fe:talc (top view) obtained from ab initio calculations. **d** Raman spectrum of the characteristic Mg-OH and Fe-OH vibrations (black line) for Fe:talc, in comparison to minnesotaite (red line; reprinted from Wang et al.⁴⁰). Inset of **d** presents an optical micrograph of the Fe:talc flake from which the spectrum is reported. **e** WDS spectrum of the Fe K α line, compared to a reference spectrum of an iron-poor talc flake with similar thickness. Inset of **e** presents a WDS map (scale bar 5 μm) of the Fe K α line. **f** SAED pattern of a ~20 layer suspended flake (200 kV, ~250 nm beam diameter). The diffraction pattern was recorded after the suspended flake was stored for more than 24 months under ambient conditions. Labeled diffraction peaks were identified by modeling of the SAED pattern of talc. The inset of **f** shows a 10 × 10 nm² atomic-resolution TEM image of the same sample.

flakes of talc (Mg,Fe)₆Si₈O₂₀(OH)₄, from here on referred to as Fe:talc. Within the investigated samples, the molar Fe/(Fe+Mg) ratio varied between 0.08 and 0.16. Talc and vermiculite monolayers have been previously reported^{7,44–48}, however, without exploring their magnetic properties in the monolayer limit⁴⁹.

RESULTS

Fe:talc structural analysis

Fe:talc samples were obtained from a mineral aggregate consisting predominantly of hematite (Fe₂O₃) and magnetite (Fe₃O₄). An optical micrograph of a polished cross-section of the mineral aggregate is provided in the Supplementary Fig. 1. Fe:talc bulk samples under study were found in the cracks of Fe₂O₃ and Fe₃O₄ platelets, hence, the Fe-rich environment allowed for much higher Fe content than that of pure natural talc minerals, where the Fe/(Fe+Mg) ratio is usually below 0.02³⁹. The flakes of Fe:talc were prepared by micromechanical exfoliation^{1,47}. The exfoliation procedure served to separate Fe:talc flakes from Fe₂O₃ and Fe₃O₄ platelets and to further thin the samples (see Methods section and Supplementary Fig. 2).

Figure 1a presents an optical micrograph of several Fe:talc flakes deposited on a SiO₂/Si chip. Optical contrast was enhanced to allow for better visibility of the thin flakes⁴⁷. Inset of Fig. 1a shows an atomic force microscopy (AFM) topography image of a Fe:talc monolayer. Figure 1b shows the height cross-section (marked by the dashed line in the inset of Fig. 1a), where a step-function fit indicates a monolayer flake with a height of about 1.7 nm. Considering the crystal structure of talc (see side view in

Fig. 1b), the monolayer thickness is expected to be 0.95 nm. The observed larger height can be attributed to a water-air mixture layer trapped between the flake and the SiO₂/Si substrate⁵⁰. A top view of the Fe:talc monolayer crystal structure is provided in Fig. 1c, considering Fe/(Fe+Mg) = 1/12.

A Raman spectrum of OH modes in Fe:talc is presented in Fig. 1d, and compared to the reported spectrum of minnesotaite⁴⁰. The presence of the satellite OH mode, which matches well the Fe-OH modes of minnesotaite, indicates that Fe is present in the samples and that it substitutes Mg in the central octahedral site. The presented spectrum was recorded from a ~12-layer flake supported by highly oriented pyrolytic graphite (HOPG). Comparison between the Raman spectra of reference talc and Fe:talc is provided in Supplementary Fig. 3. Besides the main Mg-OH mode at 3678 cm⁻¹ – which is also present in iron-poor talc – in the case of Fe:talc samples, a satellite Fe-OH mode was observed at 3662 cm⁻¹. In some cases, an additional OH mode was also observed at 3693 cm⁻¹. These modes are not observed in the case of reference Fe-poor talc (Fe/(Fe+Mg) < 0.02). The satellite OH modes are connected to a structural distortion, which introduces a non-equivalence in the sites of the OH groups and is associated with Fe substitution of Mg⁴⁰. No difference in Raman spectra was observed between freshly prepared Fe:talc flakes, and the samples aged for over 24 months in ambient conditions. Characteristic Raman modes related to vibrations of Fe/Mg in the central octahedral site and the mode related to vibrations of Si in the tetrahedral site are presented in Supplementary Fig. 3. The spectrum is compared to the spectra of hematite and magnetite. No characteristic modes of iron-oxides were observed in neither

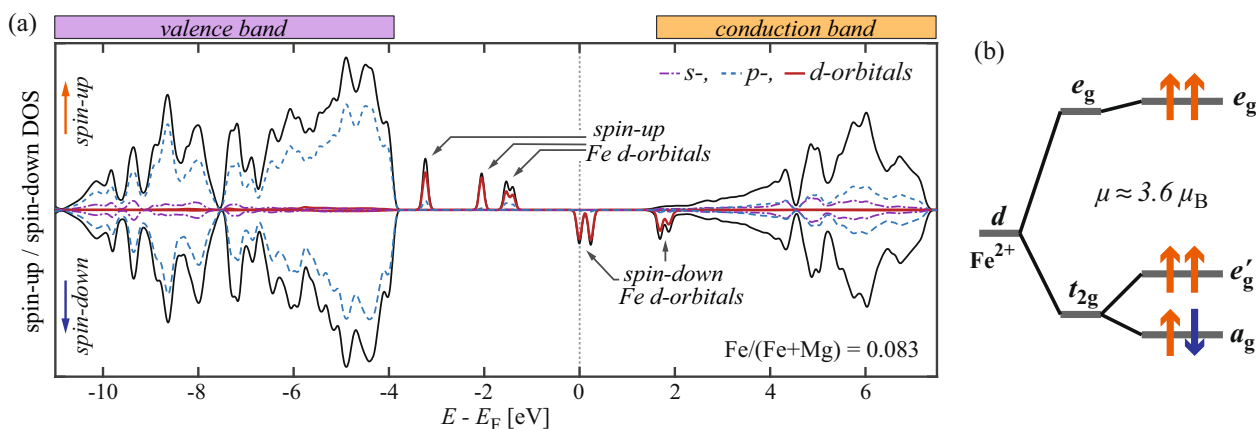


Fig. 2 Localized moment of Fe in Fe:talc. **a** spin-resolved total DOS of Fe:talc (solid black lines), obtained by a DFT calculation. Fe d -orbitals are highlighted, which contribute to the localized moment of $\sim 3.6 \mu_B$ per Fe atom. **b** Crystal field diagram (exchange splitting not shown explicitly) of the local Fe d states in Fe:talc.

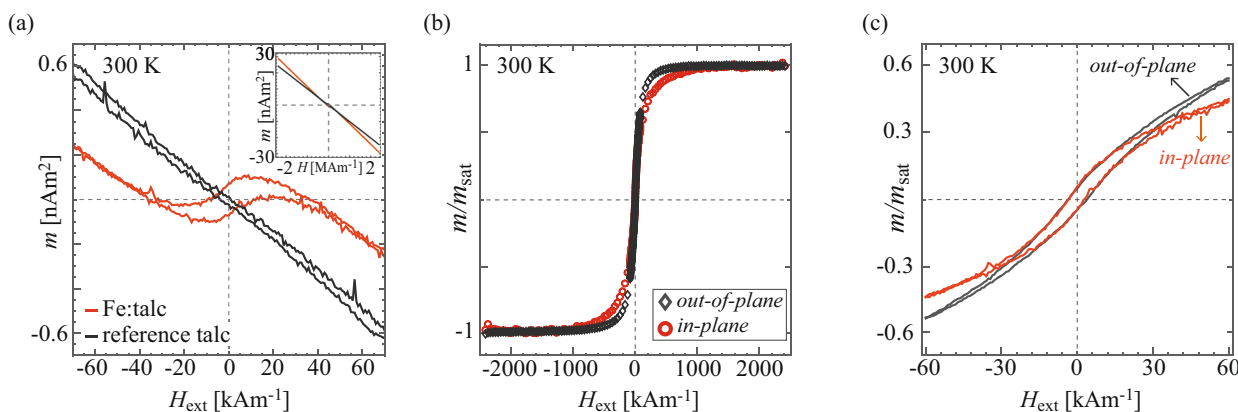


Fig. 3 Long-range magnetic ordering in Fe:talc. **a** Raw in-plane SQUID data of Fe:talc (orange) and reference talc (black), with larger H -range figure in the inset of **a**. The different slopes in the inset originate from the difference in the size of the supporting silicon substrates. **b** Background-corrected and normalized to saturation magnetization curves of Fe:talc are depicted, measured with in-plane (red dots) and out-of-plane (gray diamonds) orientation of the H -field. **c** Enlarged region of **b** near zero H -field showing both in-plane (orange lines) and out-of-plane (black lines) responses.

thin nor bulk Fe:talc flakes, therefore excluding a possibility of trapped or intercalated iron-oxide particles within the samples.

To directly prove that Fe atoms are present in these samples and to quantify the $Fe/(Fe+Mg)$ ratio, electron probe micro analysis (EPMA) was applied. An example of a wavelength dispersive X-ray spectroscopy (WDS) scan is presented in Fig. 1e. The WDS signal of the $Fe-K_{\alpha}$ line is shown for Fe:talc and is compared to the reference talc of similar size and thickness. Besides a clear confirmation of Fe in the structure, WDS allowed for the quantification of the $Fe/(Fe+Mg)$ ratio.

To demonstrate that the samples are fully stable under ambient conditions, selected area electron diffraction (SAED) patterns were recorded from suspended Fe:talc flakes after being stored in air for over 24 months (Fig. 1f). The obtained SAED patterns match the simulated ones of pure talc well. Even though both, top and bottom surfaces of the flake, were exposed to the ambient air and humidity, the diffraction pattern clearly confirms that Fe:talc is a fully air-stable material. No degradation of the samples' crystal structure was observed on any of the examined flakes.

Ab initio calculations

To clarify the electronic state of the Fe ions dissolved in talc, numerical calculations of the system were performed using density functional theory (DFT). The calculations of talc with Mg

substituted by Fe reveal that Fe ions always end up in a d^6 electronic configuration with a very robust local magnetic moment of $\sim 3.6 \mu_B$, corresponding to a $S = 4$ spin state. The local state is practically independent of the number of other Fe ions at nearest-neighbor sites as well as of the Fe content (see Supplementary Fig. 4). The corresponding total and orbitally resolved spin-up and spin-down density of states (DOS) for Fe:talc with $Fe/(Fe+Mg) = 0.083$ is presented in Fig. 2a. The d -states of Fe reside well-localized inside the band gap and they are only weakly hybridized with surrounding oxygen p states. Moreover, the degeneracy of t_{2g} and e_g states of the Fe^{2+} ions in the octahedral crystal field is lifted by a trigonal distortion (and, to a lesser extent, by the inequivalence of oxygen ions bonded with hydrogen and silicate groups). This results in a splitting of the t_{2g} states into a singlet a_g , and a doublet e'_g (Fig. 2b), with the ground state having mostly a_g character, in accordance with earlier Mössbauer studies^{41,42}.

Macroscopic magnetic response of bulk Fe:talc

The magnetic response of bulk-like Fe:talc samples were probed by superconducting quantum interference device (SQUID) magnetometry. For this purpose, several thicker flakes were transferred onto diamagnetic SiO_2/Si substrates (see Methods). The measured data were corrected for the dia- and paramagnetic

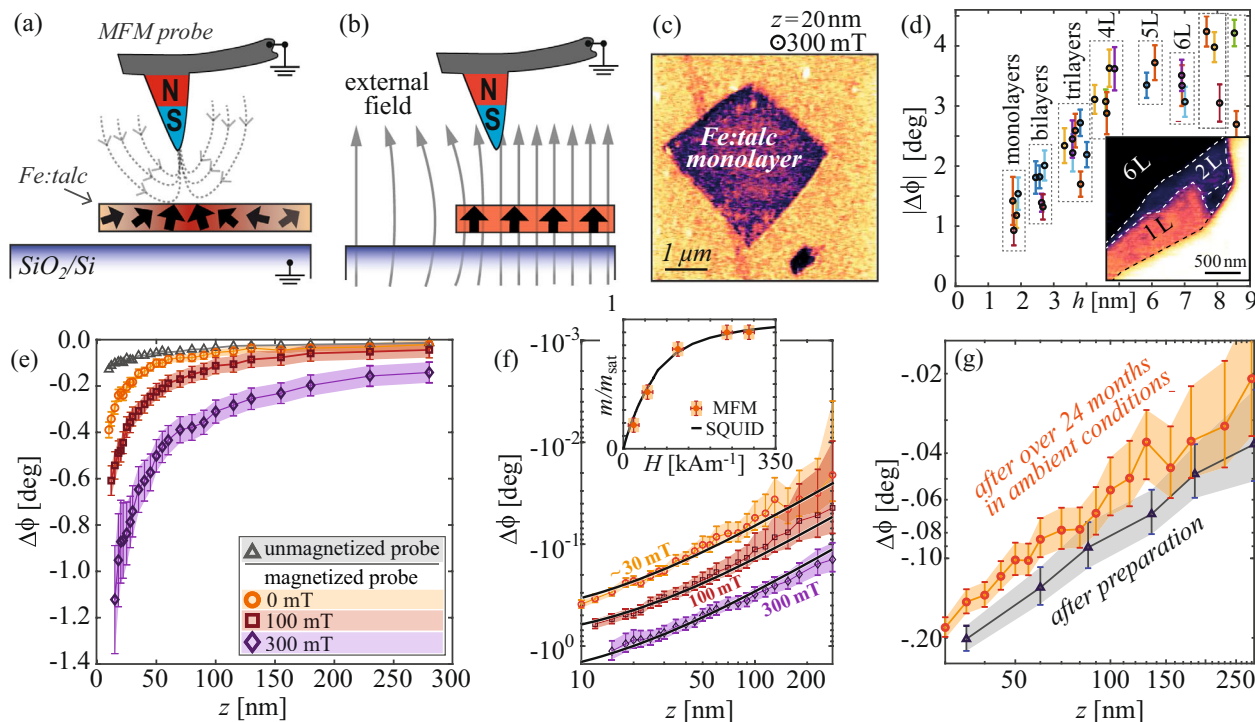


Fig. 4 Magnetic response of Fe:talc monolayers. **a, b** sketches the zero-field and applied-field MFM setups, respectively. **c** In-field (300 mT) second-pass phase lag map of a monolayer sample from Fig. 1 ($5 \times 5 \mu\text{m}^2$, lift height 20 nm, ϕ -scale 2°). **d** Thickness dependent MFM response $|\Delta\phi(h)|$ of Fe:talc, measured in 300 mT applied external field and with 20 nm lift height. Inset of **d** presents one example of the observed thickness-dependent response from several layers on the same flake. **e** $\Delta\phi(z)$ for a monolayer flake considering non-magnetized probe (gray triangles), magnetized probe in 0 mT (orange circles), 100 mT (red squares), and 300 mT fields (purple diamonds). **f** Fits (solid lines) to the magnetized probe measured data versus lift height from **e** presented in double-logarithmic scale. Inset of **f** presents a comparison to the out-of-plane SQUID magnetization curve (solid black line) and the magnetization values extracted from fitting the $\Delta\phi(z)$ MFM data with varied external fields (orange circles), also indicating error-bars of the MFM experiments. **g** Ambient stability of the MFM response of a monolayer flake, presenting (in double-logarithmic scale) $\Delta\phi(z)$ measured right after the sample preparation (gray triangles), compared to the response of the same flake after over 24 months aging under ambient conditions (orange circles).

backgrounds of the sample holders. Figure 3a provides uncorrected raw data of in-plane SQUID measurements at room temperature, comparing Fe:talc and reference talc samples. A clear magnetic response is discernible for iron-rich talc, in contrast to the purely diamagnetic behavior of the iron-poor talc sample. Figure 3b shows in-plane and out-of-plane responses to applied external fields at room temperature after background subtraction and normalization to saturation magnetization at 2400 kAm^{-1} . Saturation magnetization was achieved in-plane at fields of 1000 kAm^{-1} and out-of-plane at $\sim 500 \text{ kAm}^{-1}$. With respect to the total volume of the sample (estimated by subsequent AFM measurements), a saturation magnetization of $(11.4 \pm 2.7) \mu_{\text{B}} \text{ nm}^{-3}$ was obtained. Further, taking into account the expected Fe/(Fe + Mg) ratio provides an estimate of the local moment of iron of $(4.32 \pm 1.08) \mu_{\text{B}}$, which is in agreement with the predicted $S = 4$ spin state.

Considering the observed response, the sample exhibits weak ferromagnetic behavior at room temperature. Similar results were observed for both, in-plane and out-of-plane magnetic responses. A coercivity (H_{C}) of $3.4 \pm 0.5 \text{ kAm}^{-1}$ was observed. The origin of the weak ferromagnetic response is most likely connected to the Fe concentration (in the case of the sample shown in Fig. 3 Fe/(Fe + Mg) = 0.10 ± 0.03), the distribution of Fe in the Mg sublattice of talc, and formation of Fe-rich domains of different sizes. The results on the Fe distribution within the talc matrix are provided later in the text. Similar trends of the magnetic ordering with respect to the concentration of the dopant were observed in the cases of diluted magnetic semiconductor monolayers^{33–36}. Low-temperature measurements (at 10 K) show no significant

difference in the H_{C} and the remanence of the hysteresis loop (Supplementary Fig. 5). Based on the available mineral aggregate source, it was not possible to controllably vary the Fe concentration and examine the influence on the $M(H)$ loops. This would be possible with several different mineral sources exploring the iron-rich talc family of minerals as vermiculates and minnesotaite^{7,40–42}.

Magnetic response of Fe:talc monolayers

To probe the magnetic response of Fe:talc in the monolayer limit, two-pass magnetic force microscopy (MFM) measurements were performed with varied external out-of-plane magnetic fields under ambient conditions. Figure 4a, b schematically presents the two MFM experimental setups, without and with applied external fields respectively. In the case without applied external fields, the field of the MFM probe magnetizes the sample and the resulting contrast in the second-pass phase lag signal originates from the work related to sample magnetization⁵¹. The magnetic origin of the signal (in the case without externally applied magnetic fields) was confirmed by systematically comparing the second-pass phase lag signals recorded from magnetized MFM and non-ferromagnetic, conductive probes (see Supplementary Fig. 6). In the case when out-of-plane external magnetic fields are applied (Fig. 4b), a saturated magnetic probe responds to the difference in the field line density, which is introduced by the sample.

Figure 4c presents the second-pass phase lag map (at 20 nm lift height, with applied external out-of-plane magnetic fields of 300 mT) obtained on the monolayer flake depicted also in Fig. 1. Since mechanical exfoliation yields flakes of various thicknesses¹,

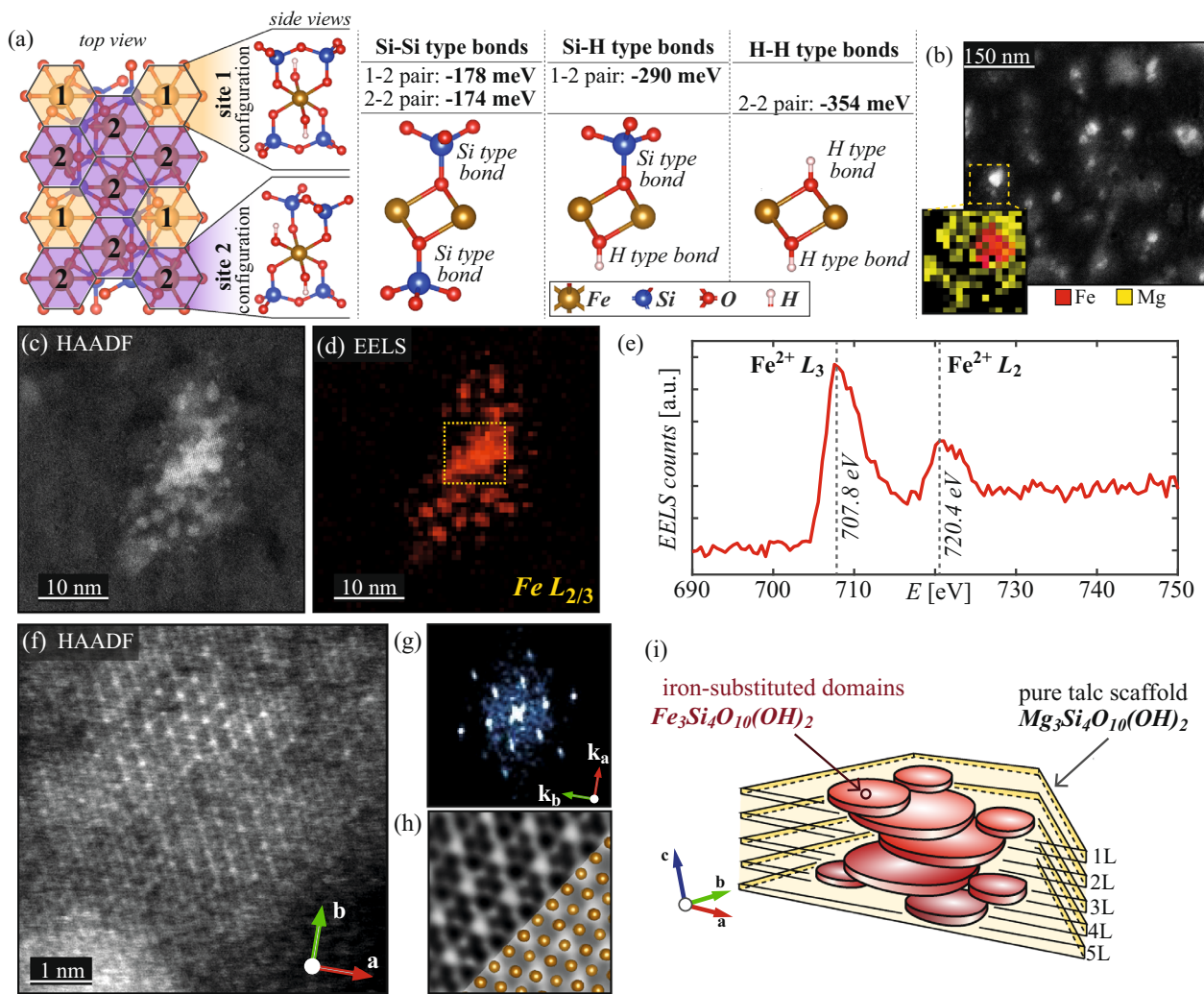


Fig. 5 Clustering of Fe in Fe:talca. **a** Pair interaction energies of Fe atoms for four distinct Fe-Fe bond types. **b** A low-magnification ($525 \times 525 \text{ nm}^2$) HAADF image of a suspended ~ 5 -layer Fe:talca flake. Inset of **b** shows an EDXS map of one bright region – Fe-rich cluster – observed in the HAADF map (Fe - red; Mg - yellow). **c** High-resolution HAADF image of one Fe-rich cluster, and its corresponding EELS map (**d**), for Fe $L_{2/3}$ line. **e** ELNES of Fe L_3 and L_2 lines, collected from the marked $10 \times 10 \text{ nm}^2$ area in **d**. Dashed vertical lines correspond to the literature values reported for Fe^{2+} ⁵⁷. **f** $6 \times 6 \text{ nm}^2$ HAADF image of a Fe-rich domain with resolved Fe sub-lattice (unit vectors are also indicated). **g** $20 \times 20 \text{ nm}^{-2}$ 2D fast Fourier transformation (FFT) of **f**, and **h** $2 \times 2 \text{ nm}^2$ FFT-filtered **f** depicting a reconstruction of the Fe sub-lattice with superimposed structural model of a Fe:talca multi-layer (bottom-right). **i** A sketch of Fe-rich regions in the case of a multi-layer flake illustrating Fe-substituted domains (red disks) in the talc scaffold (yellow).

it was possible to probe the layer dependence of the observed contrast in the second-pass phase lag signals ($\Delta\phi$) as a function of the flake thickness (h). Figure 4d presents a summary of over 20 different flakes on several SiO_2/Si chips (different colors of the error bars indicate different samples), considering the flakes below 10 nm thickness. In some cases, multiple step-heights were available on the same flake (inset of Fig. 4d). With the increase in thickness, a stronger MFM response was observed. The layer-dependent response was observed to increase linearly with an increasing number of layers (with a slope of $\sim 0.8 \text{ }^\circ\text{nm}^{-1}$) up to about four layers ($\sim 5 \text{ nm}$ flake thickness). For the thicker flakes, only a slightly stronger response as a function of thickness was observed, with a slope of $\sim 0.1 \text{ }^\circ\text{nm}^{-1}$. The WDS data points to uniformly distributed Fe among the layers of bulk-like flakes, as the thinner samples provided comparably smaller intensities of the Fe- K_α line, while also yielding similar Fe/(Fe + Mg) ratios. However, it cannot be excluded that Fe ions are non-uniformly distributed among the layers, especially when thicker flakes are considered.

A detailed MFM analysis was carried out by repeatedly scanning one line of the monolayer/substrate step along a $6\text{-}\mu\text{m}$ -long stripe (see also Supplementary Fig. 9). The sample/substrate difference in the second-pass phase lag ($\Delta\phi$) was recorded as a function of the second-pass lift height (z) and applied external magnetic fields in the range from 100 mT to 350 mT. Figure 4e presents $\Delta\phi(z)$ curves, comparing a non-magnetized probe with a magnetized probe in 0 mT, 100 mT, and 300 mT fields⁵². The results clearly demonstrate increasing attraction with increasing external magnetic field. Measurements using a more compliant⁵³, conductive n-doped silicon probe with- and without-applied-field on the same flake show no difference in the recorded phase signals (see Supplementary Fig. 7). A complementary series of with- and without-applied-field MFM measurements on a reference iron-poor talc monolayer (see Supplementary Fig. 8) yielded no significant influence of the applied field on the $\Delta\phi(z)$ curves. Measurements with unmagnetized probes (gray triangles in Fig. 4e) are mostly depending on non-magnetic contributions to $\Delta\phi(z)$, such as trapped and mirror charges and work function differences⁵⁴. Given the comparatively small phase lag obtained

by the unmagnetized probe, these have negligible influence on the observed magnetic response of the samples⁵³.

Modeling of the MFM-tip/sample interaction in dependence of the applied external magnetic fields was carried out (see Supplementary Figs. 9 and 10) to obtain semi-qualitative values of a monolayer magnetization as a function of the applied fields. Figure 4f presents (in double-logarithmic scale) the modeling results in the case of the experiments from Fig. 4e. Recorded data points are following a z^{-1} behavior, as predicted by the model. Although the measured values of the $\Delta\phi(z)$ are not taken as absolutes, they should scale with the strength of external out-of-plane fields in accordance with the out-of-plane SQUID data presented in Fig. 3. The relation between the fitted phase differences on the same sample in different external fields allows for a qualitative, relative estimate of the samples' magnetization⁵⁵. The qualitative agreement between SQUID and MFM with external out-of-plane fields applied is depicted in the inset of Fig. 4f. Considering the model for the magnetized probe without an applied external field (see Methods section and notes related to Supplementary Fig. 9), the equivalent field introduced by the probe can be estimated to be about (30 ± 20) mT.

In order to demonstrate ambient stability of Fe:talcs magnetic response in the monolayer limit, $\Delta\phi(z)$ -curves of the same monolayer flake (without applied external fields) were recorded immediately upon sample preparation and again after more than 24 months. The sample was stored in ambient conditions. Observed MFM responses are presented in Fig. 4g.

Clustering of Fe-rich domains

The ordering behavior of Fe atoms substituted in the Mg sublattice at a ratio of $\text{Fe}/(\text{Fe}+\text{Mg}) = 0.083$ was assessed by DFT calculations of pair interactions at nearest-neighbor (*NN*) sites defined as $E_{\text{pair}} = E_{\text{NN}} - E_{\text{inf}}$, where E_{NN} is the energy of a cell (see notes related to Supplementary Fig. 4 and Supplementary Table 1 for details) with a pair of Fe atoms residing on *NN* sites, E_{inf} corresponds to the energy of two Fe atoms placed far apart. One can distinguish two different substitution sites (arbitrarily labeled as configuration 1 and 2 sites in Fig. 5a-left). Note that the difference between configurations 1 and 2 can be explained considering that configuration 2 lacks inversion symmetry with respect to the Mg/Fe site in the central octahedron, which is present in configuration 1. The two sites that could accommodate Fe-Mg substitution result in four different *NN* pairs (i.e., four different configurations of the bonds via which the Fe atoms in the neighboring sites are connected), and their interaction energies are given in Fig. 5a-right. For all pairs, the energy is negative, implying attraction between Fe ions. The calculations thus strongly suggest clustering tendencies for Fe atoms. Such behavior was expected only for $\text{Fe}/(\text{Fe} + \text{Mg})$ ratios above 0.6⁵⁶, however, the distribution of Fe in talc has not been directly probed within naturally formed (close to thermodynamic equilibrium) ultra-thin single crystals at the nanoscale.

Therefore, the ordering behavior was further studied using STEM. Having iron as an element with higher *Z* than the surrounding talc matrix enables enhanced contrast of Fe-rich clusters by high-angle annular dark-field (HAADF) imaging. A low-magnification HAADF image is provided in Fig. 5b, obtained on a ~5-layer thick Fe:talcs flake. STEM-EDXS mapping (inset of Fig. 5b) was used to confirm that the bright regions in HAADF contrast correspond to Fe-rich domains (red) in the Mg-rich matrix (yellow). The average size of the Fe-rich domains was estimated to be (24 ± 10) nm from the HAADF images. The ratio of the projected surface area of these domains to the image size correlates well with the $\text{Fe}/(\text{Fe}+\text{Mg})$ ratio obtained by WDS analysis. A representative high-resolution HAADF image of one individual Fe-rich region is presented in Fig. 5c. The corresponding electron energy loss spectroscopy (EELS) elemental map, based on the Fe $L_{2/3}$ edge signal, is presented in Fig. 5d. High-resolution EELS and HAADF

maps revealed further segregation of Fe within these Fe-rich clusters. The size of the smaller Fe domains within the Fe-rich cluster was found to be (1.8 ± 0.7) nm. To exclude potential STEM beam damage effects that could introduce the formation of the small Fe-rich clusters, HAADF images were recorded both before and after EELS mapping (which introduces a rather large electron dose). The results indicate that upon TEM beam exposure smaller clusters tend to segregate, however, the general nanoscale features of Fe-rich domains in talc remain unchanged (see also Supplementary Figs. 11 and 12).

Furthermore, electron-energy loss near-edge fine structure (ELNES) analysis revealed that within these domains Fe is predominantly in a 2^+ oxidation state. An ELNES spectrum of the Fe L_3 and L_2 lines is presented in Fig. 5e. The spectrum was taken from a $10 \times 10 \text{ nm}^2$ area marked in Fig. 5d. The positions of the peaks, their relative difference, and especially the pronounced asymmetry – broadened towards higher energies – all point to predominantly Fe^{2+} ⁵⁷, which is also in accordance with the calculations.

To confirm that the observed Fe-rich domains are stable and not only the surrounding talc matrix, high-resolution HAADF images resolving the Fe sub-lattice were obtained on the samples that were exposed to the ambient conditions for over 12 months. Figure 5f provides an example of the resolved Fe sub-lattice of a Fe-rich domain. The 2D-FFT (Fig. 5g) shows tri-fold symmetry with respect to the Fe sites, yielding a distance between the neighboring Fe ions of (3.073 ± 0.012) Å. The obtained Fe sub-lattice parameter is about 1.4% larger than expected for pure talc, which is consistent with the parameters of minnesotaite, where the distance between the neighboring Fe ions is about 1.8% larger than in the case of Mg ions in pure talc³⁹. Further, the FFT-filtered reconstruction of the HAADF image from Fig. 5f is presented in (h). The reconstructed Fe sub-lattice is superimposed to a structural model of a 5-layer Fe:talcs flake, considering the basal-plane projection and showing only Fe ions. The stacking order of layers in talc explains the two concentric hexagons observed in the FFT image, as the Fe ions in the layer below would appear in between the two ions of the layer above when projected to the basal plane. An additional HAADF image and its FFT analysis are provided in Supplementary Fig. 13, resolving the Fe sub-lattice of a separate Fe-rich domain within the same suspended Fe:talcs flake. The same crystallographic orientation – with respect to the STEM scan axis – was observed in the two separate Fe-rich domains.

Taking into account the observed Fe distribution with HAADF imaging, it is likely that Fe in talc forms almost fully Fe-substituted domains, appearing as disks in individual layers which do not completely correlate between the neighboring layers. A sketch of the likely arrangement of Fe-substituted domains within a cluster is depicted in Fig. 5i, for the case of a 5-layer sample.

DISCUSSION

Talc is known to be an excellent scaffold to incorporate iron via substitution of Mg^{39–43,56}. Our results demonstrate that incorporated Fe ions are in a very robust high spin state $S = 4$ and that a weak ferromagnetic ordering is retained at room temperature. All of the presented results were obtained on samples with ages (from preparation) ranging from several hours up to more than two years. The samples were stored under ambient conditions, and no sample degradation was observed with any of the reported experimental techniques. Moreover, we show that Fe:talcs layered crystals can be thinned down to one monolayer thereby preserving their air stability and magnetic ordering in the 2D limit. We have confirmed that Fe is indeed incorporated into the talc lattice via Mg substitution, as evident from the observed Fe-OH Raman mode and atomically resolved Fe sub-lattice with HAADF STEM imaging. The substitution of Mg with Fe is further supported by the maintained stoichiometry of the samples (obtained via quantitative WDS analysis) and by the observed 2^+ oxidation

state of Fe by STEM EELS. Our finding opens a very promising pathway for tailored intrinsic magnetic monolayers via integration of Fe and potentially other magnetic ions as Ni and Co. This approach is not only valid for talc but it can easily be extended to various classes from the phyllosilicate scaffold family.

For the probed Fe/(Fe+Mg) concentration range, Fe:talc exhibits weak ferromagnetic behavior at room temperature, which is likely connected to the formation of Fe-rich domains. Within the talc group of phyllosilicates, minnesotaite $\text{Fe}_3^{2+}\text{Si}_4\text{O}_{10}(\text{OH})_2$ is the iron-rich end member and is reported to be a layered antiferromagnet in the bulk^{41,42}. However, high-crystallinity samples of minnesotaite are extremely rare, and usually intertwined with other phases of the mineral aggregate, making isolation and exfoliation of monolayers very challenging.

Large “bulk” single crystals of the phyllosilicates, which can incorporate Fe, are found within the mica group^{7,39,40,43}. Biotites $\text{K}(\text{Mg},\text{Fe})_3(\text{AlSi}_3\text{O}_{10})(\text{F},\text{OH})_2$ with annite $\text{KFe}_3^{2+}(\text{AlSi}_3\text{O}_{10})(\text{OH})_2$ as the iron-rich end member of the biotite mica group – also known as “black micas” – could be considered as analogs to talc and minnesotaite^{39,40}. A common point for all the phyllosilicates are their aluminate/silicate tetrahedra $[\text{AlSi}_3\text{O}_{10}]$ that could be seen as encapsulation for the central octahedral, in which magnetic properties could be tailored and preserved.

For magnetic phyllosilicates to be employed in future technological applications, it is needed to establish scalable fabrication routes for high-crystallinity thin films. Synthetic mica single crystals are available⁵⁸, and their magnetic properties are starting to attract the attention of the scientific community⁴³. Research on synthetic talc is mostly focused on applications where large-area single-crystals are not a priority⁵⁹. Hydrothermal methods are one of the common routes to produce synthetic talc^{59,60}, yielding high-purity and high-crystallinity samples with lateral crystal sizes of up to few micrometers. Hydrothermal synthesis of talc with controlled substitution of Mg with Ni, and Co was demonstrated⁶¹. However, growth methods for crystalline ultra-thin films suitable for applications in magnetoelectronics and magneto-optics are lacking.

Lastly, Fe:talc and most of the mentioned Fe-rich members of the phyllosilicate family are magnetic insulators. In the case of Fe:talc, this is evident from the DOS calculations presented in Fig. 2 (see also Supplementary Fig. 4). The bandgap of ~6 eV – obtained by the calculations – matches well to the literature values^{44–46}. Breakdown voltages of pure talc are in the order of 1 Vnm^{-1} , and are comparable to both conventionally used and vdW dielectrics⁴⁶. Especially when considering vdW spin-filter heterostructures realized with CrI_3 ⁶², Fe:talc, and the other Fe-rich layered silicate magnetic insulators are very interesting candidates for demonstrating giant tunneling magneto-resistance effect in tunneling junctions and for the integration into magnetoresistive random access memories^{27,62}.

METHODS

Preparation of Fe:talc flakes

The flakes of Fe:talc were prepared by micromechanical exfoliation, starting from a natural mineral aggregate, which predominantly consists of hematite (Fe_2O_3) and magnetite (Fe_3O_4); see also Supplementary Fig. 1 and the associated notes. Within cracks, and mainly along grain boundaries and (0001) cleavage planes of hematite, fluorite (CaF_2), and the van der Waals mineral Fe:talc were found. In the most likely scenario, the Fe-rich environment within the cracks of the hematite and magnetite provides the source of Fe substituting Mg in the talc structure, consequently forming Fe:talc crystals⁵⁶.

Small crystals from the mineral aggregate – ~500 μm in size – were initially spread over a glass slide. Thin hematite platelets were selected by optical microscopy, appearing semi-transparent and with dark-red color. Selected platelets were picked up by a micromanipulator and deposited onto a sticky tape (Nitto Denko ELP BT150ECM); see also Supplementary Fig. 2. After multiple peeling against two pieces of the tape, the material was deposited on SiO_2/Si chips (300 nm oxide layer), and the tape was slowly peeled off. Since hematite platelets cannot be exfoliated in this

process, only pre-existing splitting along the basal (0001) crystal faces and cracks allow for the further separation of the platelets, which enables access to Fe:talc formed within. Hematite platelets were very rarely observed deposited on the substrates after the transfer and were easily identified by optical microscopy. With this process, and with the particular mineral aggregate, the largest isolated Fe:talc crystals were found to be ~200 μm in diameter, and up to 1 μm thick. The thinnest flakes observed were monolayers (1 nm thick).

Raman spectroscopy

A Horiba LabRam HR Evolution confocal Raman spectrometer was used with EMCCD detector, 532.1 nm laser (100 mW power on the sample surface), $\times 100$ magnification lens, 1800 grooves mm^{-1} , and confocal hole of 100 μm . The acquisition time was varied from 20 s in the case of bulk (above 100 nm thickness), up to 1200 s for the flakes thinner than 10 nm. No sample damage was observed after prolonged exposure to the laser beam, confirmed by subsequent measurements of Raman spectra and by AFM. The modes observed in the range from 150 cm^{-1} to 700 cm^{-1} , are attributed to Mg/Fe vibrations within the central $[(\text{Mg},\text{Fe})\text{O}_4(\text{OH})_2]$ octahedral, while the modes above 3600 cm^{-1} correspond to the vibrations of the OH groups⁴⁰.

EPMA and WDS investigation

A Jeol superprobe equipped with five wavelength dispersive spectrometers was used for EPMA quantitative analysis and element mapping. Samples were coated with a ~10 nm carbon layer. Analyses were carried out in WDS mode with focused electron beam, 10–100 nA beam currents, 10–15 kV analyzing voltages, and counting times ranging from 10 s to 300 s. The standards used for calibration were kaersutite for Mg and Si K_α lines, and magnetite for the Fe K_α line. ZAF correction was applied to account for inter-element effects. Standard deviations in percentage for Mg, Si, and Fe were 0.37, 0.60, and 1.86, respectively. Since the flakes were prepared from a natural mineral source, specimens from each batch of flakes were analyzed to ensure batch-to-batch reproducibility and to determine the Fe/(Fe + Mg) ratio.

SQUID magnetometry measurements

Since SQUID magnetometry is an integral technique, special care was taken with Fe:talc sample preparation for SQUID measurements. Exclusively plastic or carbon pincers, blades, and sample holders were used during both, sample and substrate preparation. In order to have sufficient volume of the material for SQUID experiments, several “bulk-like” Fe:talc flakes were selected and transferred on the same $2 \times 2\text{ mm}^2$ SiO_2/Si chips. The total volume of transferred Fe:talc flakes per sample were in the range of $1000\text{--}5000\ \mu\text{m}^3$ for Fe-rich talc, and $10,000\text{--}100,000\ \mu\text{m}^3$ for the reference Fe-poor talc. Prior to SQUID experiments, all observed flakes on the surface were checked by Raman spectroscopy to confirm that only Fe:talc is present. The sample volume was determined by AFM.

Hysteresis loops were recorded using the superconducting quantum interference device - vibrating sample magnetometer (SQUID-VSM) MPMS2 from Quantum Design. $M(H)$ curves were measured at 300 K and 10 K with the in-plane magnetic field ranging from -2393.1 kAm^{-1} to 2393.1 kAm^{-1} . For the measurements of the samples out-of-plane magnetization loops, compensation of the magnetic field offset was carried out by shifting the x -axis of the $M(H)$ loops by 1.46 kAm^{-1} (i.e., 0.07% of the total measurement range). Magnetic field offset was negligibly small in the case of the in-plane measurements, and therefore its compensation was not carried out. The sample background was estimated by fitting raw magnetization data m_{raw} with the following heuristic description of the measured data (1)⁶³:

$$m_{\text{raw}}(H) = d - kH + B(H) + \frac{k_1}{2}(1 - \text{Erf}(k_2(H \pm H_c))), \quad (1)$$

where the first two terms represent diamagnetic contributions, the second term $B(H)$ is the Brillouin function representing paramagnetic behavior and the last term is a heuristic function approximating ferromagnetic response to external fields H . As the sample holder used in out-of-plane measurements is made of a weakly paramagnetic material, we used SQUID measurements of iron-poor reference talc to estimate the sample-holders magnetic signal employing the equation above. Subsequently, the paramagnetic out-of-plane contribution of the sample holder was subtracted from appropriate Fe:talc SQUID measurements. Finally, subtraction of the diamagnetic terms yielded the corrected SQUID data presented here.

STEM investigations and sample preparation

For the transfer of the flake on TEM grids (200-nm-thick holey SiN membranes from Norcada Inc.) an all dry viscoelastic transfer, based on polypropylene carbonate stamps was performed⁶⁴. High-resolution TEM and SAED were carried out on a JEOL JEM2200FS operating at 200 kV. To confirm the talc crystal structure, image simulations were performed using the JEMS software package. High-resolution STEM experiments were performed on a probe-corrected FEI Titan³ G2 60–300 microscope, equipped with a Fischione HAADF detector (Model 3000). The electron energy was set to 300 keV. Furthermore, a Gatan Quantum energy filter with a Gatan K2 direct electron detection camera for electron energy loss spectroscopy (EELS) was used (Supplementary Fig. 12).

MFM experiments

AFM and MFM experiments were conducted on a Horiba/AIST_NT Omegascope AFM under ambient conditions. For MFM, TipsNano MFM01 probes were used with CoCr coating (~40 nm tip curvature radius, ~70 kHz resonance, ~5 N/m force constant, $m_p \approx -1.5 \cdot 10^{-16} \text{ Am}^2$)⁶⁵. The n-doped silicon probes used for confirmation measurements were NanoSensors PPP-LFMR probes (~10 nm tip curvature radius, ~20 kHz resonance, ~0.5 Nm^{-1} force constant). Metallic, non-ferromagnetic PtI-coated Electrical Force Microscopy (EFM) probes of type ACCESS-EFM, AppNano, (~30 nm tip curvature radius, ~63 kHz resonance, ~2.7 Nm^{-1} force constant) were used for initial validation of the samples' magnetic response (see Supplementary Fig. 6). All MFM probes were subjected to an external out-of-plane magnetic field with a magnetic flux density of ~330 mT for over 20 min prior to the MFM experiments. Cross-checks of the probes' magnetic response were carried out on MFM test samples. In-field measurements were performed on a custom-made sample stage, which allowed easy insertion and removal of permanent magnets. The out-of-plane character of the applied external magnetic field, as well as its flux density, were confirmed at the sample position with a Hall-probe (M-Test MK4, Maurer Magnetic AG). MFM line-scans were conducted in a two-pass regime, with the second-pass lift-height varied from 20 nm to 280 nm (Supplementary Fig. 9). To confirm stability during measurements, height variations in line scans were performed in succession at a given field. AFM topography and MFM phase maps were processed using Gwyddion v2.55, an open source SPM analysis software. For MFM phase maps, zero-order row correction was applied, and the mean value of the phase, which corresponds to the SiO_2/Si substrate, was set to zero.

Calculations

DFT calculations were performed using the projector augmented waves (PAW) method⁶⁶ as implemented in the Vienna Ab-initio Simulation Package (VASP)^{67–69}. Generalized gradient approximation with the Perdew-Burke-Ernzerhof parameterization for solids⁷⁰ was employed as an exchange-correlation functional, as it was shown to give the best-relaxed structure for talc⁷¹. Atomic positions were relaxed to the accuracy in forces of 0.01 $\text{eV}\text{\AA}^{-1}$. For the simulation of the low-Fe content sample, we started with a unit cell of talc (space group C_1)⁷², consisting of a single MgO layer with one of the 12 Mg atoms substituted by an Fe atom, as shown in Fig. 1b. This corresponds to a Fe/(Fe + Mg) ratio of $1/12 \approx 0.083$. There are two distinct substitution sites as shown in Fig. 4a but the magnetic moment is practically the same for both of them. Additional calculations for intermediate and high Fe content (results are shown in Supplementary Fig. 4), 25%, 50%, 75%, were performed in a doubled unit cell to better satisfy constraints for a random configuration of substituted sites. The calculation for 100% of Fe was performed in the original talc unit cell.

DATA AVAILABILITY

The datasets obtained and analyzed during the study are available from the corresponding authors on reasonable request.

CODE AVAILABILITY

Computer codes employed during the study are available from the corresponding authors on reasonable request.

Received: 6 August 2021; Accepted: 30 November 2021;
Published online: 21 December 2021

REFERENCES

- Novoselov, K. S. et al. Electric field effect in atomically thin carbon films. *Science* **306**, 666–669 (2004).
- Novoselov, K. S., Mishchenko, O. A., Carvalho, O. A. & Neto, A. C. 2D materials and van der Waals heterostructures. *Science* **353**, 9439 (2016).
- Castellanos-Gomez, A. Why all the fuss about 2D semiconductors? *Nat. Photon.* **10**, 202–204 (2016).
- Okano, S. et al. Voltage-controlled dielectric function of bilayer graphene. *Adv. Opt. Mater.* **8**, 2000861 (2020).
- Matković, A. et al. Interfacial band engineering of MoS₂/gold interfaces using pyrimidine-containing self-assembled monolayers: toward contact-resistance-free bottom-contacts. *Adv. Electron. Mater.* **6**, 2000110 (2020).
- Todorović, D. et al. Multilayer graphene condenser microphone. *2D Materials* **2**, 045013 (2015).
- Frisenda, R., Niu, Y., Gant, P., Muñoz, M. & Castellanos-Gomez, A. Naturally occurring van der Waals materials. *npj 2D Mater. Appl.* **4**, 38 (2020).
- González-Herrero, H. et al. Atomic-scale control of graphene magnetism by using hydrogen atoms. *Science* **352**, 437–441 (2016).
- Červenka, J., Katsnelson, M. I. & Flipse, C. F. J. Room-temperature ferromagnetism in graphite driven by two-dimensional networks of point defects. *Nat. Phys.* **5**, 840–844 (2009).
- Son, Y. W., Cohen, M. L. & Louie, S. G. Energy gaps in graphene nanoribbons. *Phys. Rev. Lett.* **97**, 216803 (2006).
- Bonilla, M. et al. Strong room-temperature ferromagnetism in VSe₂ monolayers on van der Waals substrates. *Nat. Nanotechnol.* **13**, 289–293 (2018).
- Avsar, A. et al. Defect induced, layer-modulated magnetism in ultrathin metallic PtSe₂. *Nat. Nanotechnol.* **14**, 674–678 (2019).
- Li, B. et al. A two-dimensional Fe-doped SnS₂ magnetic semiconductor. *Nat. Commun.* **8**, 1958 (2017).
- Fu, S. et al. Enabling room temperature ferromagnetism in monolayer MoS₂ via in situ iron-doping. *Nat. Commun.* **11**, 2034 (2020).
- Chen, M. et al. Ferromagnetic behaviors in monolayer MoS₂ introduced by nitrogen-doping. *Appl. Phys. Lett.* **116**, 073102 (2020).
- Huang, B. et al. Layer-dependent ferromagnetism in a van der Waals crystal down to the monolayer limit. *Nature* **546**, 270–273 (2017).
- Gong, C. et al. Discovery of intrinsic ferromagnetism in two-dimensional van der Waals crystals. *Nature* **546**, 265–269 (2017).
- Fei, Z. et al. Two-dimensional itinerant ferromagnetism in atomically thin Fe₃GeTe₂. *Nat. Mater.* **17**, 778–782 (2018).
- Li, H., Ruan, S. & Zeng, Y. J. Intrinsic van der Waals magnetic materials from bulk to the 2D limit: new frontiers of spintronics. *Adv. Mater.* **31**, 1900065 (2019).
- Lee, J. et al. Structural and optical properties of single- and few-layer magnetic semiconductor CrPS₄. *ACS Nano* **11**, 10935–10944 (2017).
- Zhang, W., Wong, P. K. J., Zhu, R. & Wee, A. T. Van der Waals magnets: wonder building blocks for two-dimensional spintronics? *InfoMat* **1**, 479–495 (2019).
- May, A. F. et al. Ferromagnetism near room temperature in the cleavable van der Waals crystal Fe₅GeTe₂. *ACS Nano* **13**, 4436–4442 (2019).
- Wang, H. et al. Above room-temperature ferromagnetism in wafer-scale two-dimensional van der Waals Fe₃GeTe₂ tailored by a topological insulator. *ACS Nano* **14**, 10045–10053 (2020).
- Shcherbakov, D. et al. Raman spectroscopy, photocatalytic degradation, and stabilization of atomically thin chromium tri-iodide. *Nano Lett.* **18**, 4214–4219 (2018).
- Awschalom, D. D. & Flatté, M. E. Challenges for semiconductor spintronics. *Nat. Phys.* **3**, 153–159 (2007).
- Han, W., Kawakami, R. K., Gmitra, M. & Fabian, J. Graphene spintronics. *Nat. Nanotechnol.* **9**, 794–807 (2014).
- Mak, K. F., Shan, J. & Ralph, D. C. Probing and controlling magnetic states in 2D layered magnetic materials. *Nat. Rev. Phys.* **1**, 646–661 (2019).
- Park, J. G. Opportunities and challenges of two-dimensional magnetic van der Waals materials: magnetic graphene? *J. Phys. Cond. Matter* **28**, 301001 (2016).
- Tan, C. et al. Gate-controlled magnetic phase transition in a van der Waals magnet Fe₅GeTe₂. *ACS Nano* **21**, 5599–5605 (2021).
- Gish, J. T. et al. Ambient-stable two-dimensional CrI₃ via organic-inorganic encapsulation. *ACS Nano* **15**, 10659–10667 (2021).
- Tu, Z. et al. Ambient effect on the Curie temperatures and magnetic domains in metallic two-dimensional magnets. *npj 2D Mater. Appl.* **5**, 54 (2021).
- Tiwari, S., Van de Put, M. L., Sorée, B. & Vandenberghe, W. G. Magnetic order and critical temperature of substitutionally doped transition metal dichalcogenide monolayers. *npj 2D Mater. Appl.* **5**, 62 (2021).
- Chen, R. et al. Tunable room-temperature ferromagnetism in Co-doped two-dimensional van der Waals ZnO. *Nat. Commun.* **12**, 3952 (2021).
- Zhang, F. et al. Monolayer vanadium-doped tungsten disulfide: a room-temperature dilute magnetic semiconductor. *Adv. Sci.* **7**, 2001174 (2020).

35. Pham, Y. T. H. et al. Tunable ferromagnetism and thermally induced spin flip in Vanadium-doped tungsten diselenide monolayers at room temperature. *Adv. Mater.* **32**, 2003607 (2020).
36. Yun, S. J. et al. Ferromagnetic order at room temperature in monolayer WSe₂ semiconductor via vanadium dopant. *Adv. Sci.* **7**, 1903076 (2020).
37. Wang, S., Wang, J. & Khazaei, M. Discovery of stable and intrinsic antiferromagnetic iron oxyhalide monolayers. *Phys. Chem. Chem. Phys.* **22**, 11731–11739 (2020).
38. Niu, Y. et al. Mechanical and liquid phase exfoliation of cylindrite: a natural van der Waals superlattice with intrinsic magnetic interactions. *2D Materials* **6**, 035023 (2019).
39. Bideaux, R. A., Bladh, K. W., Nichols, M. C., Anthony, J. W. *Handbook of Mineralogy: Silica, Silicates* (Mineral Data Publishing, Tucson, 2005).
40. Wang, A., Freeman, J. J. & Jolliff, B. L. Understanding the Raman spectral features of phyllosilicates. *J. Raman Spectrosc.* **46**, 829–845 (2015).
41. Ballet, O., Coey, J. M. D. & Burke, K. J. Magnetic properties of sheet silicates; 2:1:1 layer minerals. *Phys. Chem. Minerals* **12**, 370–378 (1985).
42. Ballet, O., Coey, J. M. D., Mangin, P. & Townsend, M. G. Ferrous talc-a planar antiferromagnet. *Solid State Commun.* **55**, 787–790 (1985).
43. Ma, Z., Skumryev, V. & Gich, M. Magnetic properties of synthetic fluorophlogopite mica crystals. *Mater. Adv.* **1**, 1464–1471 (2020).
44. Alencar, A. B., Barboza, A. P. M., Archanjo, B. S., Chacham, H. & Neves, B. R. Experimental and theoretical investigations of monolayer and few-layer talc. *2D Materials* **2**, 015004 (2015).
45. Mania, E. et al. Spontaneous doping on high quality talc-graphene-hBN van der Waals heterostructures. *2D Materials* **4**, 031008 (2017).
46. Barcelos, I. D. et al. Infrared fingerprints of natural 2D talc and plasmon-phonon coupling in graphene-talc heterostructures. *ACS Photonics* **5**, 1912–1918 (2018).
47. Vasić, B. et al. Two-dimensional talc as a van der Waals material for solid lubrication at the nanoscale. *Nanotechnology* **32**, 265701 (2021).
48. Zou, Y. C. et al. Ion exchange in atomically thin clays and micas. *Nat. Mater.* **20**, 1677–1682 (2021).
49. Gradwohl, K. P. *Exfoliation And Characterization Of Natural Two-dimensional Magnetic Flakes*, Master Thesis (University of Leoben, 2018).
50. Matković, A. et al. Spectroscopic imaging ellipsometry and Fano resonance modeling of graphene. *J. Appl. Phys.* **112**, 123523 (2012).
51. Körnig, A., Hartmann, M. A., Teichert, C., Fratzl, P. & Faivre, D. Magnetic force imaging of a chain of biogenic magnetite and Monte Carlo analysis of tip-particle interaction. *J. Phys. D Appl. Phys.* **47**, 235403 (2014).
52. Schreiber, S. et al. Magnetic force microscopy of superparamagnetic nanoparticles. *Small* **4**, 270–278 (2008).
53. Angeloni, L. et al. Experimental issues in magnetic force microscopy of nanoparticles. *AIP Conf. Proc.* **1667**, 020010 (2015).
54. Li, L. H. et al. Dielectric screening in atomically thin boron nitride nanosheets. *Nano Lett.* **15**, 218–223 (2015).
55. Angeloni, L. et al. Single nanoparticles magnetization curves by controlled tip magnetization magnetic force microscopy. *Nanoscale* **9**, 18000–18011 (2017).
56. Corona, J. C., Jenkins, D. M. & Dyar, M. D. The experimental incorporation of Fe into talc: a study using X-ray diffraction, Fourier transform infrared spectroscopy, and Mössbauer spectroscopy. *Contrib. Mineral. Petrol.* **170**, 29 (2015).
57. Garvie, L. A., Craven, A. J. & Brydson, R. Use of electron-energy loss near-edge fine structure in the study of minerals. *Am. Mineral.* **79**, 411–425 (1994).
58. Van Valkenburg, A. & Pike, R. G. Synthesis of mica. *J. Res. Natl Bur. Stand.* **48**, 360–369 (1952).
59. Claverie, M. et al. Synthetic talc and talc-like structures: preparation, features and applications. *Chem. Eur. J.* **24**, 519–542 (2018).
60. Dumas, A. et al. Phyllosilicates synthesis: a way of accessing edges contributions in NMR and FTIR spectroscopies. Example of synthetic talc. *Phys. Chem. Mineral.* **40**, 361–373 (2013).
61. Wilkins, R. W. T. & Ito, J. Infrared spectra of some synthetic talcs. *Am. Mineral.* **52**, 1649–1661 (1967).
62. Song, T. et al. Giant tunneling magnetoresistance in spin-filter van der Waals heterostructures. *Science* **360**, 1214–1218 (2018).
63. O'Hara, D. J., Zhu, T. & Kawakami, R. K. Importance of paramagnetic background subtraction for determining the magnetic moment in epitaxially grown ultrathin van der Waals magnets. *IEEE Magn. Lett.* **9**, 1405805 (2018).
64. Pizzocchero, F. et al. The hot pick-up technique for batch assembly of van der Waals heterostructures. *Nat. Commun.* **7**, 11894 (2016).
65. Corte-León, H. et al. Comparison and validation of different magnetic force microscopy calibration schemes. *Small* **16**, 1906144 (2020).
66. Blöchl, P. E. Projector augmented-wave method. *Phys. Rev. B* **50**, 17953 (1994).
67. Kresse, G. & Joubert, D. From ultrasoft pseudopotentials to the projector augmented-wave method. *Phys. Rev. B* **59**, 1758 (1999).
68. Kresse, G. & Hafner, J. Ab initio molecular dynamics for liquid metals. *Phys. Rev. B* **47**, 558 (1993).
69. Kresse, G. & Furthmüller, J. Efficient iterative schemes for ab initio total-energy calculations using a plane-wave basis set. *Phys. Rev. B* **54**, 11169 (1996).
70. Perdew, J. P. et al. Restoring the density-gradient expansion for exchange in solids and surfaces. *Phys. Rev. Lett.* **100**, 136406 (2008).
71. Tunega, D., Bučko, T. & Zaoui, A. Assessment of ten DFT methods in predicting structures of sheet silicates: Importance of dispersion corrections. *J. Chem. Phys.* **137**, 114105 (2012).
72. Perdikatsis, B. & Burzlaff, H. Strukturverfeinerung am talk Mg₃(OH)2Si₄O₁₀. *Z. Kristallogr. Cryst. Mater.* **156**, 177–186 (1981).

ACKNOWLEDGEMENTS

This work is supported by the Austrian Science fund (FWF) via 2020 START programme (grant no. Y1298 N), by the FWF Lise Meitner fellowship (grant no. M2323 N36), and by an FWF ANR International programme (grant no. I1788 N20). We acknowledge financial support by the “Zukunftsfonds Steiermark” for the K2 camera and funding from the European Union’s Horizon 2020 research program under Grant Agreement No. 823717 ESTEEM3. The authors acknowledge infrastructural support of the Montanuniversität Leoben (Raman AFM TERS lab). O.E.P. acknowledges the financial support under the scope of the COMET program within the K2 Center “Integrated Computational Material, Process and Product Engineering (IC-MPPE)” (Project No 859480). This program is supported by the Austrian Federal Ministries for Climate Action, Environment, Energy, Mobility, Innovation and Technology (BMK) and for Digital and Economic Affairs (BMDW), represented by the Austrian research funding association (FFG), and the federal states of Styria, Upper Austria and Tyrol.

AUTHOR CONTRIBUTIONS

Mineral aggregate was provided by K.P.G.; A.M., L.L., and K.P.G. carried out the sample preparation, Raman spectroscopy, AFM, and MFM characterization, and with M.K. and C.T. interpreted AFM and MFM data. L.L. developed the setup for in-field MFM and did the modeling of the MFM data. Mineral aggregate cross-sections were prepared and analyzed by M.Z., J.R., and R.B.; O.P. and L.R. carried out the calculations. M.Z. and A.M. performed EPMA/WDS characterization and with R.B., K.P.G., C.T., and J.R. discussed EPMA and Raman data. A.S. carried out SQUID experiments, and with G.S. and D.R.T.Z. interpreted SQUID data. J.G. with A.L. prepared the samples for STEM experiments. E.F. and D.K. carried out STEM analysis and with A.M., C.T., and F.H. interpreted the STEM results. C.G. carried out SAED experiments and with A.M. analyzed the data. A.M. compiled all the data. A.M., L.L., O.P., and C.T. wrote the manuscript. All authors discussed the results and reviewed the manuscript.

COMPETING INTERESTS

The authors declare no competing interests.

ADDITIONAL INFORMATION

Supplementary information The online version contains supplementary material available at <https://doi.org/10.1038/s41699-021-00276-3>.

Correspondence and requests for materials should be addressed to Aleksandar Matković or Christian Teichert.

Reprints and permission information is available at <http://www.nature.com/reprints>

Publisher's note Springer Nature remains neutral with regard to jurisdictional claims in published maps and institutional affiliations.



Open Access This article is licensed under a Creative Commons Attribution 4.0 International License, which permits use, sharing, adaptation, distribution and reproduction in any medium or format, as long as you give appropriate credit to the original author(s) and the source, provide a link to the Creative Commons license, and indicate if changes were made. The images or other third party material in this article are included in the article’s Creative Commons license, unless indicated otherwise in a credit line to the material. If material is not included in the article’s Creative Commons license and your intended use is not permitted by statutory regulation or exceeds the permitted use, you will need to obtain permission directly from the copyright holder. To view a copy of this license, visit <http://creativecommons.org/licenses/by/4.0/>.